Remote Sensing of Environment 157 (2015) 111–122

Contents lists available at ScienceDirect

Remote Sensing of Environment

journal homepage: www.elsevier.com/locate/rse

Two-stream remote sensing model for water quality mapping: 2SeaColor

Mhd. Suhyb Salama [a,b,*], Wouter Verhoef [a]

[a] University of Twente, Faculty of Geo-Information Science and Earth Observation (ITC), Department of Water Resources, P.O. Box 217, 7500 AE Enschede, The Netherlands
[b] SMART HYDROLOGY (www.smarthydrology.com), Elbertbos 10, 7545 GV Enschede, The Netherlands

ARTICLE INFO

Article history:
Received 22 January 2014
Received in revised form 10 July 2014
Accepted 18 July 2014
Available online 14 August 2014

Keywords:
Radiative transfer
Downwelling attenuation coefficient
Turbid waters
2SeaColor
Lake Naivasha

ABSTRACT

A fundamental measure to characterize water quality is the attenuation coefficient for downward planar irradiance in the water column. In this paper we present an analytical forward model and develop an inversion scheme (2SeaColor) to retrieve the downwelling attenuation coefficients from remote sensing data. The forward formulation of 2SeaColor provides an analytical and stable solution of the direct and diffuse components of the radiative transfer equation. The common high turbidity of inland waters is accounted for in 2SeaColor by projecting its effect on the inherent optical properties (IOPs) using the similarity transform. The inversion scheme of 2SeaColor uses a novel approach to parameterize the spectral dependency of IOPs. In this parameterization 2SeaColor uses the curvature information of observed remote sensing spectra to deduce the spectral-shape of the total absorption coefficient.

The forward model is verified using simulated data from the International Ocean Colour Coordinating Group (IOCCG data) and is compared with two existing models.

Statistical analysis results of model verification show that the forward model is able to derive K_d values with 3% accuracy (relative mean absolute error). Our solution provides an improvement on the accuracy of the estimated K_d when compared to other models, and especially at larger depths. The inversion scheme is validated against three sets of data: IOCCG, field measured and satellite observed matchups. Field measurements were collected in the turbid Naivasha Lake, Kenya. The mean absolute relative error in the derived K_d in all data sets did not exceed 15%, with the satellite matchup set resulting in the largest discrepancy.

The developed model, 2SeaColor, is stable to noise up to 15% and consistently produces accurate results which make it an ideal candidate model for the future Ocean and Land Colour Instrument (OLCI) on board the Sentinel-3 mission.

1. Introduction

A fundamental measure of water quality is the downwelling attenuation coefficient for planar irradiance, which is a cumulative indicator of the biogeochemical properties and activities of the water column (Scheffer et al., 2009). The downwelling attenuation coefficient (K_d) depends on the composition of the medium and slightly on the directional structure of the ambient light field and thus provides a relationship between biology and optics (Kirk, 1994; Saulquin et al., 2013).

An increase in K_d means, therefore, a reduction of the light penetrating the water column, thereby affecting the functioning of the aquatic ecosystem and the transfer of heat and gases at the atmosphere–water boundary layer (Bilotta and Brazier, 2008; Giardino et al., 2001; Manizza et al., 2004; Kettle and Merchant, 2008; Lewis et al., 1990; Morel and Antoine, 1994; Uiboupin and Sipelgas, 2007).

Remote sensing data over water are related to the physical and biological properties of water constituents through inherent optical properties (IOPs). These IOPs characterize the absorption and scattering of the water column and determine, thus, the downwelling attenuation coefficient, K_d.

There are two types of models to derive K_d from remote sensing data. The first is a radiance-based model that estimates K_d from a band ratio. The second type of model derives the IOPs of the water constituents, and then estimates K_d from the retrieved IOPs, hereafter called IOP-based models.

Austin and Petzold (1981) pioneered the development of an algorithm to derive K_d from ocean color radiometric data using the radiance-based model. This model is based on a power–law empirical relationship between $K_d(490)$ and the blue–green ratio ($\lambda_1 = 443$ nm, $\lambda_2 = 550$ nm). This model has been modified over time to suit the spectral bands of different sensors. For instance, O'Reilly et al. (1998) derived chlorophyll-a concentration from the blue–green ratio and then related

* Corresponding author at: University of Twente, Faculty of Geo-Information Science and Earth Observation (ITC), Department of Water Resources, P.O. Box 217, 7500 AE, Enschede, The Netherlands. Tel.: +31 640353056.
E-mail addresses: s.salama@utwente.nl, salama@smarthydrology.nl (M.S. Salama).

http://dx.doi.org/10.1016/j.rse.2014.07.022
0034-4257/

it to K_d using empirical coefficients. Mueller (2000) adapted the Austin & Petzold model to derive $K_d(490)$ from Sea Wide Field of view Sensor (SeaWiFS) data, whereas Kratzer et al. (2008) revised it to retrieve $K_d(490)$ from Medium Resolution Imaging Spectrometer (MERIS) data.

In the IOP-based models, the attenuation coefficient is estimated from the inherent optical properties (IOPs) of water constituents.

With the advent of remote sensing techniques, many semi-analytical IOP-based models were developed to derive the attenuation coefficient with a high degree of accuracy (Lee et al., 2005a; Lee et al., 2005b, 2007). Research studies on uncertainties showed, however, that over turbid water the forward water-model, i.e. the formulation that describes light attenuation in the water, contributes more than 45% of uncertainty to the total error budget on derived IOPs and thus K_d (Lee et al., 2010; Salama and Stein, 2009; Wang et al., 2005a; Wang et al., 2005b). While most efforts focused, so far, on improving the atmospheric correction as a separate component in the processing chain (Antoine and Morel, 1999; Chomko et al., 2003; Frouin and Pelletier, 2007; Salama et al., 2004; Salama and Shen, 2010a; Wang and Gordon, 1994; Wang et al., 2005a,b, 2009), little has been done to improve the forward model for radiative transfer in water. Despite the importance of the forward model, most, if not all, studies neglect water turbidity and employ the (quasi) single scattering approximation (Gordon et al., 1975; Gordon et al., 1988; Maritorena et al., 2002; Lee et al., 2002; Van der Woerd and Pasterkamp, 2008; Salama et al., 2009; Salama and Shen, 2010b). Recently, Gege (2012) developed an analytic model for the direct and diffuse components of the downwelling irradiance in the water column. The direct and diffuse downwelling coefficients were, however, approximated as a linearly weighted sum of the absorption and backscattering coefficients, which holds for clear water only.

Therefore, and in preparation for the operational component of the Copernicus program, the Sentinel 2 and 3 missions, there is an urgent need to develop a reliable retrieval model that improves the estimation of the downwelling attenuation coefficient in turbid waters.

In this paper we expand on a previously applied model (e.g. Shen et al., 2010) by developing the 2SeaColor model: a forward remote sensing model with an inversion scheme for turbid waters. The proposed model provides an analytical and stable solution of the direct and diffuse components of downwelling irradiance and accounts for the high turbidity of inland waters.

2. Study area

Lake Naivasha is a high altitude lake (1890 m above sea level) located in the East African Rift Valley, about 80 km Northwest of Nairobi, Kenya (Fig. 1). The water surface of the lake covers an area of about 145 km^2 with the average depth of 5 m. It is a freshwater lake in a closed drainage basin with no surface outlet and surrounded by four alkaline lakes (Ayenew and Becht, 2008). There are generally calm wind conditions in the morning over the lake, whereas strong winds prevail in the afternoon. During the field visit, we observed that in the afternoon wind causes sediment re-suspension and rapidly mixes the water column. The inlets of the Gilgil and Malewa Rivers supply high loads of sediment into the lake. The sediment types consist of sandy mud and brown clay with a sedimentation rate of between 1 cm per year in the central lake and 3 cm per year in the bays (Tarras-Wahlberg et al., 2002).

The concentrations of chlorophyll-a have increased from 30 $\mu g\ l^{-1}$ in 1982 to 178 $\mu g\ l^{-1}$ in 1995 and transparency has correspondingly declined to about 60 cm, but briefly rose to 160 cm in 1998–9 due to the diluting effect of the 'El Niño' rains (Harper et al., 2002).

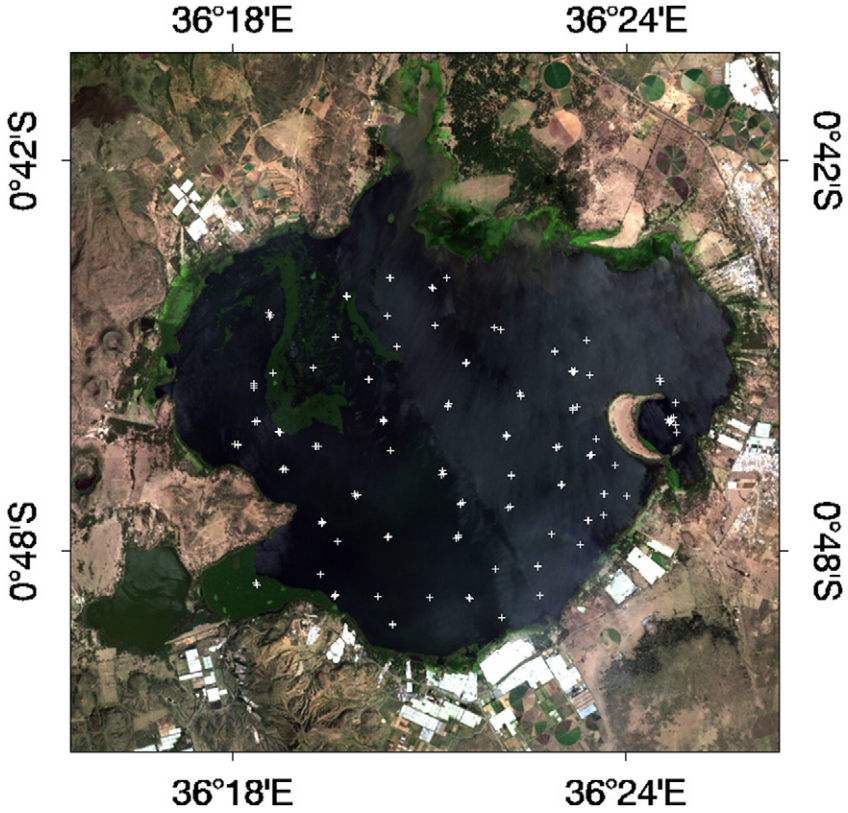

Fig. 1. False color composite (R = 655 nm, G = 562 nm, B = 482 nm) of Landsat-8 image acquired on the 25-1-2014 above the Naivasha Lake. The white-plus symbols indicate the locations of the sampled sites during the field data collection campaign.

3. Data sets

Evaluation and validation of the proposed model are carried out using three data sets: *in situ* data, earth observation matchup and simulated data sets from the International Ocean Colour Coordinating Group (IOCCG) report (Lee, 2006).

3.1. In-situ data

The *in situ* data consist of 97 measurements of above-water remote sensing reflectance and underwater downwelling planar irradiance. Fig. 1 shows the locations of the sampled sites (plus symbols) on a false color composite of a Landsat-8 image acquired on 25-1-2014 above the Lake Naivasha. The composite is formed from bands 2, 3 and 4 of Landsat-8 (R = 655 nm, G = 562 nm, B = 482 nm).

We used TriOS Ramses sensors (http://www.trios.de) to perform the radiometric measurements which included above-water upwelling radiance, above-water downwelling irradiance and underwater downwelling irradiance at two depths, 0.2 and 0.7 m. Above water measurements of upwelling radiance were performed at 42° zenith and 135° azimuth relative to the sun, whereas under water measurements were performed at nadir (following the ocean optics protocol, Mueller et al., 2003). The sun elevation was between 45° and 70° for all measurements. The remote sensing reflectance (*Rrs*) was computed from the ratio of the above-water upwelling radiance (L_u) to the above-water downwelling irradiance (E_d) as $Rrs = L_u/E_d$. The attenuation coefficient (K_d) was calculated from the underwater downwelling planar irradiances at two depths, $z_1 = 0.2\ m$ and, $z_2 = 0.7\ m$ as:

$$Ed(z_2) = Ed(z_1)\ \ln(-K_d \Delta Z).$$

Fig. 2 shows the mean values of measured *Rrs* and K_d and their ranges, i.e. max/min values.

3.2. Earth observation matchups

Earth observation matchup data consist of observations from the Medium Resolution Imaging Spectrometer (MERIS) on board Envisat. MERIS is an orbital sensor with 15 bands covering the spectral range from 400 nm to 950 nm. It operates with two spatial modes: full (FR) and reduced (RR) resolution. In this study we use three full resolution level-1b MERIS images acquired on the 20th, 23rd and 26th of September 2010. The matchups sites are selected to be ± 1 h of MERIS overpass, at the same sampling location, i.e. one pixel at the location of field sampling. In total we have 34 MERIS pixels that are concurrent with field measurements, hereafter called MERIS-matchups.

3.3. IOCCG data set

IOCCG data set is obtained from radiative transfer simulations, at 30° sun zenith, of synthesized inherent optical properties (IOPs), (Lee, 2006). IOCCG spectra were simulated assuming the solar irradiance model of Gregg and Carder (1990) and a cloud-free sky. A wind speed of 5 m/s is applied, and the water body is assumed homogeneous. Spectral bands were set from 400 nm to 750 nm, with a spacing of 10 nm. Inelastic scattering, such as Raman scattering, chlorophyll fluorescence, etc. was excluded from the simulations. More details on the IOCCG data sets can be found at http://www.ioccg.org/groups/OCAG_data.html.

4. Method

4.1. Forward formulation

Optical properties of water are usually described by means of an absorption coefficient a and a backscattering coefficient b_b, in units of m^{-1}. Radiative transfer inside the water column can be described by the two-stream radiative transfer equations (Duntley, 1942, 1963) as follows:

$$\begin{aligned} \frac{dE_s}{dz} &= kE_s \\ \frac{dE^-}{dz} &= -s'E_s + \alpha E^- - \sigma E^+ \\ \frac{dE^+}{dz} &= sE_s + \sigma E^- - \alpha E^+ \end{aligned} \quad (1)$$

where E_s is the direct solar flux, and E^- and E^+ are the diffuse downward and upward fluxes, respectively, and z is the vertical dimension and supposed to increase in upward direction and to be zero at the top, so that it is negative under water. The extinction coefficient for direct sunlight, k, is related to the absorption coefficient a and the total scattering coefficient b by: $k = c/\mu_s$, where μ_s is the cosine of underwater solar zenith angle and $c = a + b$ is the beam attenuation coefficient. The coefficients, s and s' are the backscattering and forward scattering for direct sunlight, given by $s = b_b/\mu_s$, and $s' = b_f/\mu_s$. The coefficients σ and σ' describe the diffuse backward and forward scattering and are obtained from integrating s and s' over the backward and forward directions, respectively, i.e. $\sigma = 2b_b$, $\sigma' = 2b_f$. Similarly, the diffuse extinction coefficient is called κ, and it is obtained by integrating k over a hemisphere, as $\kappa = 2c$. The coefficient α in system (1) is the diffuse extinction coefficient minus the diffuse forward scattering coefficient, σ' so that, $\alpha = \kappa - \sigma' = 2a + \sigma$. Table B.1 in Appendix B summarizes the coefficients of Eq. (1).

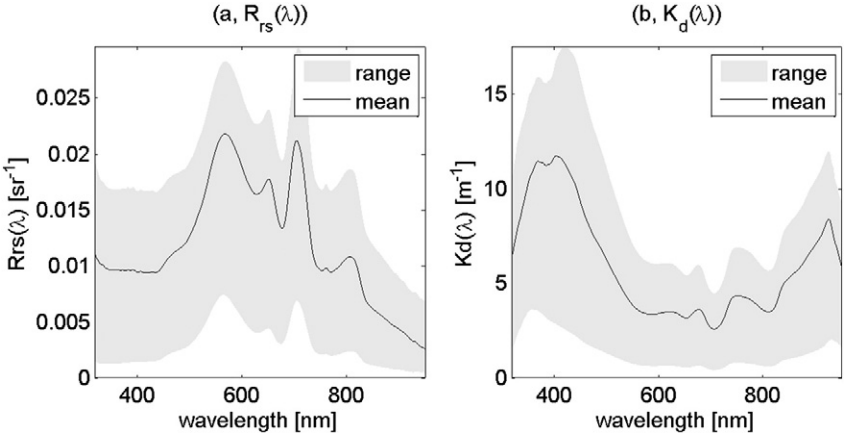

Fig. 2. Average values of measured *Rrs* and K_d (black curves) with their ranges (Max, Min) as shaded areas.

4.1.1. Similarity transformation

Suspended particles in water often exhibit a very strong forward scattering, and this peaked component of the scattered radiation might be considered as light that has not been scattered at all, and so should not be included in the beam extinction coefficient c either. However, we may assume that a fraction of the scattering in forward direction is still diffuse, similar to the backscattering.

It is known from radiative transfer theory that the reflectance of a semi-infinite medium, such as deep or very turbid water, is only a function of the backscattering coefficient and the absorption coefficient, in particular of the ratio of the two: b_b/a (Gordon et al., 1988). From this, it follows that the peaked nature of the forward scattering in the downward direction has no influence on the infinite reflectance. However, it does have an effect on the attenuation of light inside the medium, and we show that a more reliable calculation of the radiation field inside the medium can be obtained if the forward scattering peak is removed from the scattered radiation and added back to the non-scattered flux. However, doing so means that the beam extinction coefficient c, the single scattering albedo ω, and the backscattering efficiency have to be redefined, and this is done by the similarity transformation of Van de Hulst (1981), in such a way that the b_b and a are not affected, so that the reflectance remains invariant. The equations needed for this similarity transformation are given in Appendix A.

4.1.2. Solution of the two-stream radiative transfer equation

The solution of the equation system in (1), with detailed mathematical manipulations to avoid singularity, is provided in Appendix B of this manuscript.

For the top of the medium we obtain:

$$E^+(0) = r_\infty E^-(0) + r_{sd}^\infty E_s(0), \tag{2}$$

where r_∞ is the so-called infinite reflectance, which is the bihemispherical reflectance for the semi-infinite medium, and r_{sd}^∞ is the directional–hemispherical reflectance of the semi-infinite medium. They are given by:

$$r_\infty = \frac{x}{1 + x + \sqrt{1+2x}}, \tag{3}$$

and

$$r_{sd}^\infty = \frac{\sqrt{1+2x}-1}{\sqrt{1+2x}+2\mu_w}, \tag{4}$$

where x is the ratio of backscattering to absorption coefficients, so $x = b_b/a$, and μ_w is the cosine of the solar zenith angle beneath the water surface. The downward diffuse irradiance is derived as:

$$E^-(z) = E^-(0)e^{mz} + (s' + \sigma\ r_{sd}^\infty)E_s(0)J_1(k,z), \tag{5}$$

where the function J_1 is given in Eq. (B.8) of Appendix B and $m = 2\sqrt{a(a+2b_b)}$. The total downward planar irradiance of diffuse and direct light is:

$$E_d(z) = E^-(z) + E_s(0)e^{kz} \tag{6}$$

Eq. (6) does not describe a purely exponential attenuation of the planar irradiance with depth, since two extinction coefficients are involved, k and m. This was also demonstrated by Preisendorfer (1986) in his treatment of the contrast reduction theory.

However, in many cases the direct solar flux will dominate, and the attenuation will be approximately exponential.

The downwelling attenuation coefficient of diffuse and direct light is analytically differentiated with depth as:

$$K_d = \frac{1}{E_d}\frac{dE_d}{dz} \tag{7}$$

The upward diffuse irradiance is given by:

$$E^+(z) = r_\infty E^-(z) + r_{sd}^\infty E_s(z). \tag{8}$$

Obviously the expression that was found for the top of the medium also holds deeper into the medium. This holds only for a semi-infinite medium, however.

Now the irradiance reflectance just beneath the water surface is:

$$R = \frac{E^+(0)}{E_d(0)} = \frac{r_\infty E^-(0) + r_{sd}^\infty E_s(0)}{E_d(0)}, \tag{9}$$

Eq. (9) can be translated to just above the water remote sensing reflectance (Mobley, 2004):

$$Rrs = \frac{0.52R}{Q - 1.7R}, \tag{10}$$

where the parameter Q is the ratio of the water upwelling irradiance to upwelling radiance just beneath the surface.

4.2. Inversion

For remote sensing applications we proceed by firstly inverting the measured/observed spectra of remote sensing reflectance to inherent optical properties (IOPs), and secondly by calculating K_d from the derived IOPs.

Since 2SeaColor requires only the bulk absorption and backscattering coefficients to compute K_d we only need to parameterize the backscattering coefficient, b_b i.e. parameterization of chlorophyll-a and colored dissolved matter absorption are not required. In the treatment of the backscattering coefficient we make a distinction between large, $b_{bp,l}$, and small, $b_{bp,s}$, particles following (Kopelevich, 1983). The spectral dependency of the backscattering coefficient of suspended particulate matter is modeled as:

$$b_{bp}(\lambda) = b_{bp,l}(\lambda_r) \times \left(\frac{\lambda}{\lambda_r}\right)^{-y_l} + b_{bp,s}(\lambda_r) \times \left(\frac{\lambda}{\lambda_r}\right)^{-y_s}, \tag{11}$$

where λ_r stands for the reference wavelength and y_s, y_l are the spectral slopes of small and large particles respectively. The backscattering coefficient of water molecules is taken from Mobley (2004).

We first initiate the values of the spectral slopes y_s, y_l and the backscattering of large particles. The small particles' backscattering coefficient is then estimated from the observed reflectance at the near infrared (NIR ~ 735–750 nm) by assuming that the absorption at the NIR is only due to water molecules absorption (Yang et al., 2013), i.e. $a(NIR) = a_w(NIR)$.

The result predicted by the 2SeaColor model is r_∞, and this is an irradiance reflectance quantity for the semi-infinite medium, which can be approximated by Qr_{rs}, where Q ~ 3.25 (Morel and Gentili, 1996). Now r_∞ in Eq. (3) can be inverted to give the inherent optical property $x = b_b/a$ as:

$$x = \left[\left(\frac{1+r_\infty}{1-r_\infty}\right)^2 - 1\right]/2 = \frac{2r_\infty}{(1-r_\infty)^2}. \tag{12}$$

Then $b_{bp,s}(NIR) = a_w(NIR).x(NIR)$. This value is extrapolated to shorter wavelengths using Eq. (11). The total absorption coefficient is then estimated from b_b and the ratio x.

4.3. Data analysis

We use four parameters to determine the goodness-of-fit between derived and known values. These are the slope and intercept of the regression line, the coefficient of determination R^2, and the mean of absolute relative-differences (rMAD). Accurate retrievals lead to unity slope, zero intercept, unity R^2 and zero rMAD. The slope and intercept are computed using model-II regression (Laws, 1997). The value of R^2 is computed as the squared correlation coefficient between derived and known values. The mean of absolute relative-differences (rMAD) is used in this manuscript as a measure of the error in the retrievals. The rMAD value is calculated as:

$$\mathrm{rMAD} = 100\langle|1-\mathrm{derived}/\mathrm{known}|\rangle. \quad (13)$$

5. Results

5.1. Verification

5.1.1. Sensitivity to high turbidity

We use the synthesized IOPs from the IOCCG data set and generate under water irradiance reflectance from the forward calculations of four models: (i) Gordon et al. (1988), (ii), Gordon et al. (1975), (iii), Albert and Mobley (2003), and (iv) the 2SeaColor. Two values of the Q factor are used with the Gordon et al. (1988) model: (i) the parameterization of Devred et al. (2007) and (ii) the tabulated values of Zibordi and Berthon (2001). The f parameter in the Gordon et al. (1975) model is computed from the formulation of Morel and Gentili (1991). The resulting values of irradiance reflectance are compared at the blue wavelength 440 nm, with the full radiative transfer solutions provided in the IOCCG data set. The choice of the blue wavelength is to demonstrate that the 2SeaColor has improved forward calculations for water with high scattering coefficients. Further, we evaluate the performance of these models for two water types defined with respect to the beam attenuation coefficient, $c = b + a$, whereby the clear water type has its c values lower than 95% of the data and the turbid water type has its c values higher than 95% of the data (equivalent to $\bar{c} \pm 2\sigma$). This subdivision of clear and turbid water results in $c < 0.25\ \mathrm{m}^{-1}$ for clear water and $c > 6.42\ \mathrm{m}^{-1}$ for turbid water. The statistical measures of fit (rMAD) for these scenarios are shown in Table 1. Over the whole range of c values, the proposed model, 2SeaColor, outperforms all other models in producing irradiance reflectance spectra with errors (rMAD) ~5.5%. The error increases from clear (rMAd ~ 3%) to turbid waters (rMAD ~ 8%). This is also observed in the models of Gordon et al. (1975) and Albert and Mobley (2003).

The 2SeaColor model performs similarly to the model of Gordon et al. (1975) in clear waters (with small c values), for which the single scattering result is a valid approximation. On the other hand, with the increase of water turbidity, the 2SeaColor outperforms the other models. It should be emphasized, however, that the choice of the Q ratio, either tabulated (Zibordi and Berthon, 2001), or parameterized (Devred et al., 2007), greatly affects the result of the Gordon et al. (1988) model. If the Q ratio is carefully chosen, the latter model produces similar results to the 2seaColor. Therefore the rMAD values of the Gordon et al. (1988) model in Table 1 are only representative for the selected values of the Q ratio. Nonetheless, the uncertainty about which Q value to choose gives 2SeaColor an advantage over other models, as it has the ability to retrieve the Q ratio during the inversion.

5.1.2. Models inter-comparison

We use the IOCCG data set to inter-compare the forward 2SeaColor with two types of model: radiance-based (Austin and Petzold, 1981; Mueller, 2000), and IOP-based, (Lee et al., 2005a,b). Austin and Petzold (1981) estimate K_d by its empirical relationship with the ratio of water-leaving radiances at two wavelengths within the blue–green spectral region (adapted by Mueller, 2000)

$$K_d(490) = K_w(490) + 0.15645\left[\frac{R_{rs}(490)}{R_{rs}(555)}\right]^{-1.5401}, \quad (14)$$

where $K_w(490)$ is the diffuse attenuation coefficient of water molecules (~0.016 m^{-1}).

The IOP-based method of Lee et al. (2005a, their Eq. (10)) estimates K_d at depth z as a function of IOPs and the sun zenith angle as:

$$K_d(z,\ \theta_s,\ \lambda) = m_0(z,\theta_s)a(\lambda) + m_1(z,\theta_s) \times \left(1-m_2(z,\theta_s)\mathrm{e}^{-m_3(z,\theta_s)a(\lambda)}\right)b_b(\lambda), \quad (15)$$

where θ_s is the solar zenith angle in the air and the coefficients m_0, m_1, m_2 and m_3 are given in Lee et al. (2005a, their Table 2) for varying sun zenith angles and depths.

The comparison is performed for depths −0 (for Austin and Petzold, 1981 model) and −5, −10 and −20 m (for Lee et al., 2005a model).

Table 2 shows the goodness of fit parameters, computed between simulated and calculated $K_d(490)$ values from the three methods. 2SeaColor produces $K_d(490)$ values with a unity slope and a maximum rMAD = 2.76% at depth −5 m. Although the Lee et al. (2005a) model was originally developed using the same underlying model of the simulated IOCCG data set (Hydrolight, Mobley, 2004), it has produced less accurate results of K_d (rMAD 5 ~ 7%) than the 2SeaColor (rMAD 2 ~ 3 %), especially for values at deeper depths of −10 and −20 m. The resulting slopes have also a larger deviation from the unity line (2%–7% compared to 0.1% for 2SeaColor). The advantage of 2SeaColor over the Lee et al. (2005a) method is that it is fully analytical and therefore independent on tuning parameters (as those presented in Table 2 for the Lee et al., 2005a model). In contrast to these two IOP-based models (2SeaColor and Lee et al., 2005a), the radiance-based model of Austin and Petzold (1981) produced $K_d(490)$ values that are 55% off unity and have large errors, rMAD > 25 %.

Table 1
The relative mean absolute errors (rMAD, Eq. (13)) of irradiance reflectance spectra computed from five different forward calculations. The rMAd errors are also calculated with respect to clear and turbid water types with c values lower than 0.25 m^{-1} and higher than 6.42 m^{-1}, respectively.

	Gordon et al., 1988 (their Eq. (2)) $R = Q\sum_{i=1}^{2} l_i\left(\frac{b_b}{a+b_b}\right)^i$, $l_1 = 0.0949, l_2 = 0.0749$				Gordon et al. (1975) $R = f\frac{b_b}{a+b_b}$,		Albert and Mobley (2003)		2SeaColor of this work	
	Q ratio				f from Morel and Gentili (1991)		Their Eq. (8), and Table 3			
	Zibordi and Berthon (2001)		Devred et al. (2007)							
rMAD(440)	34.67		24.80		15.66		13.24		5.49	
Water types	Clear	Turbid	Clear	Turbid	Clear	Turbid	Clear	Turbid	Clear	Turbid
rMAD(440)	32.81	24.66	40.80	34.68	5.31	23.18	9.315	22.57	3.13	7.96

Table 2
Inter-comparison of the forward calculation using the IOCCG data set.

	2SeaColor				Lee et al. (2005a)			Austin and Petzold (1981)
Depth	0	−5	−10	−20	−5	−10	−20	0
Slope	1.01	1.01	1.01	1.01	0.98	0.93	0.95	0.46
Intercept × 10^{-3}	−4.46	−4.25	−1.86	2.28	−8.19	−1.00	−1.95	90.00
R^2	1.00	1.00	1.00	1.00	1.00	1.00	1.00	0.76
rMAD%	2.05	2.76	2.44	2.36	4.76	6.51	6.92	25.56

5.2. Validation of 2SeaColor inversion

The simulated, measured and observed remote sensing spectra are first inverted to the absorption and backscattering coefficients. These IOPs are then used to estimate K_d.

The unknowns, $b_{bp,l}$, y_l, y_s in Eq. (11) and η (the fraction of peaked scattering), are derived by fitting the modeled R_{rs} to the measured/observed R_{rs} using the least-squared error minimization method. The constraints are set such that they guarantee positive values of the retrieved variables. The water absorption and scattering coefficients are taken from tabulated values (Mobley, 2004; Pope and Fry, 1997).

5.2.1. IOCCG data

Fig. 3 shows the results of inverting IOCCG remote sensing spectra to IOPs and K_d using the 2SeaColor model. For all depths, the rMADs of the derived $K_d(490)$values are less than 15% with ~14% off-unit slope and an intercept of about -0.05 m^{-1} and high R^2 values (>0.98). These results show that the inversion of the above water remote sensing reflectance to obtain $K_d(490)$ has an intrinsic error of about 15% and is overestimated at the upper end of Fig. 3, i.e. moderately turbid water.

The retrieved values of IOPs, namely the bulk absorption and backscattering coefficients at 490 nm are also shown in Fig. 4.

The derived IOPs fit the synthesized IOCCG values with 12% off-unity slope with small intercept and high R^2 (>0.98). The rMAD values of both coefficients, $a(490)$ and $b_b(490)$, are below 11% and similar to the results of $K_d(490)$ in Fig. 4, i.e. overestimated at the upper end.

5.2.2. MERIS matchups and field data

5.2.2.1. Correction of MERIS images. The MERIS images are first atmospherically corrected using the *in situ* measured *Rrs* values. The top of atmosphere remote sensing reflectance Rrs_{toa}, is written as the sum (Gordon, 1997):

$$Rrs_{toa}(\lambda) = Rrs_{atm} + T\left(Rrs_{sfc} + Rrs\right), \tag{16}$$

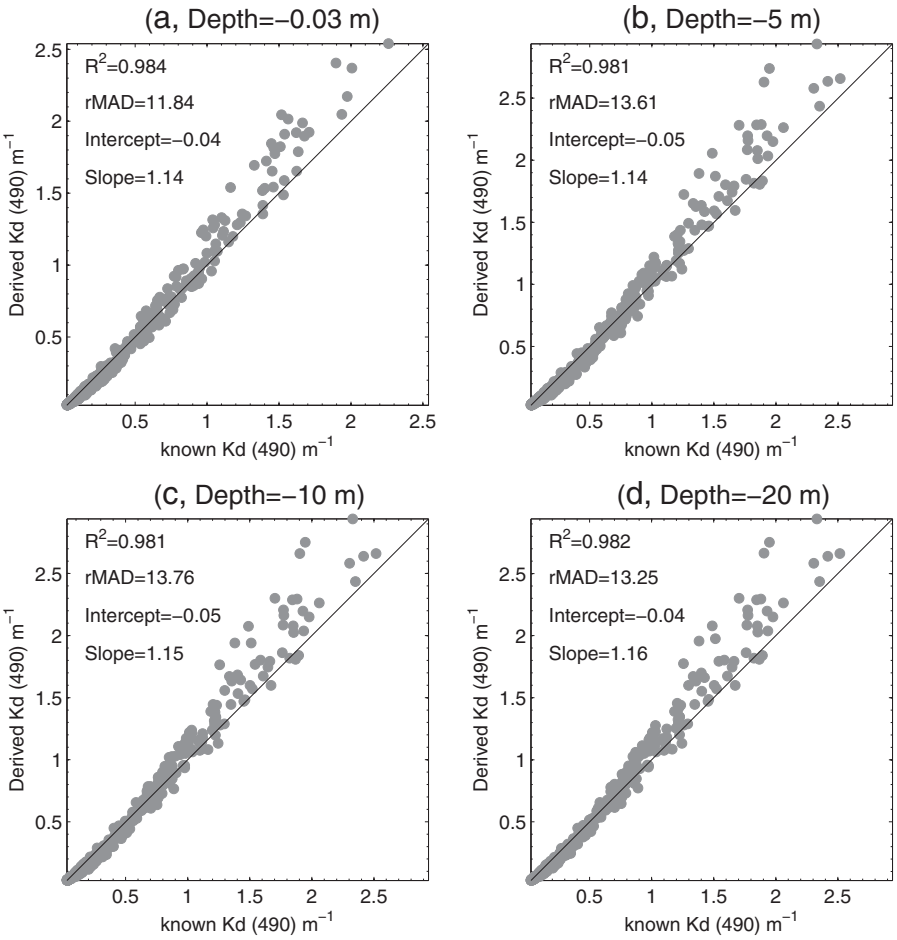

Fig. 3. The results of 2SeaColor inversion, applied to the IOCCG data set. $K_d(490)$ is derived at different depths: (a) 0, (b) 5, (c) 10 and (d) 20 m.

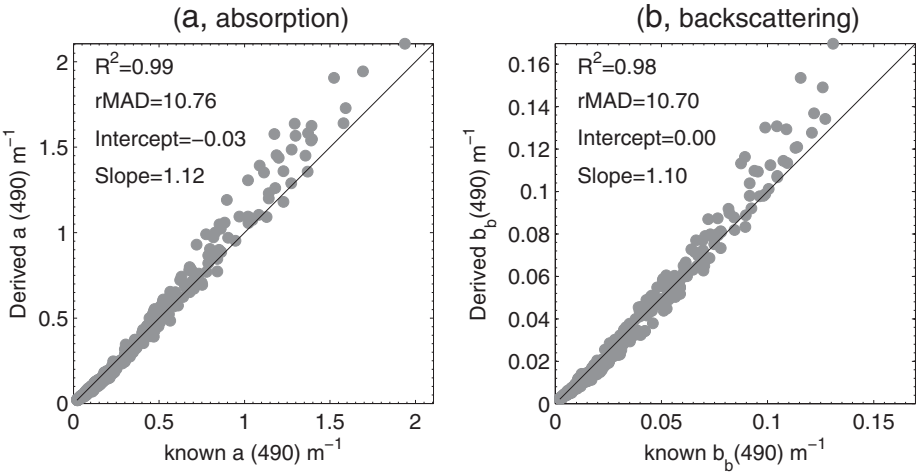

Fig. 4. Derived versus known values of IOPs of the IOCCG data set. (a): total absorption coefficient at 490 nm; (b): the total backscattering coefficient at 490 nm.

where Rrs_{atm} is the atmospheric contribution from Rayleigh and Mie scattering ($Rrs_{atm} = Rrs_r + Rrs_a$); Rrs_{sfc} is the specular component due to reflection at the water surface; Rrs is the water leaving component and T is the two-way atmospheric transmittance. The contribution of Rayleigh scattering is computed for each location (pixel) using the viewing-illumination geometry and subtracted from MERIS observed Rrs_{toa}. The specular surface reflectance is derived using the model of Cox and Munk (1954a,b) at a wind speed of 3 m/s.

The system of equations

$$Rrs_c(\lambda) = Rrs_a + TRrs_{sfc} + TRrs_w, \tag{17}$$

where $Rrs_c(\lambda) = Rrs_{total}(\lambda) - Rrs_r(\lambda)$, is then solved by substituting the measured Rrs_w, and observed Rrs_c to find, Rrs_a and T using linear regression. We used the GeoCalVal model of Salama et al. (2012) to determine the optimum calibration (Cal) and validation (Val) sets. The Cal and Val

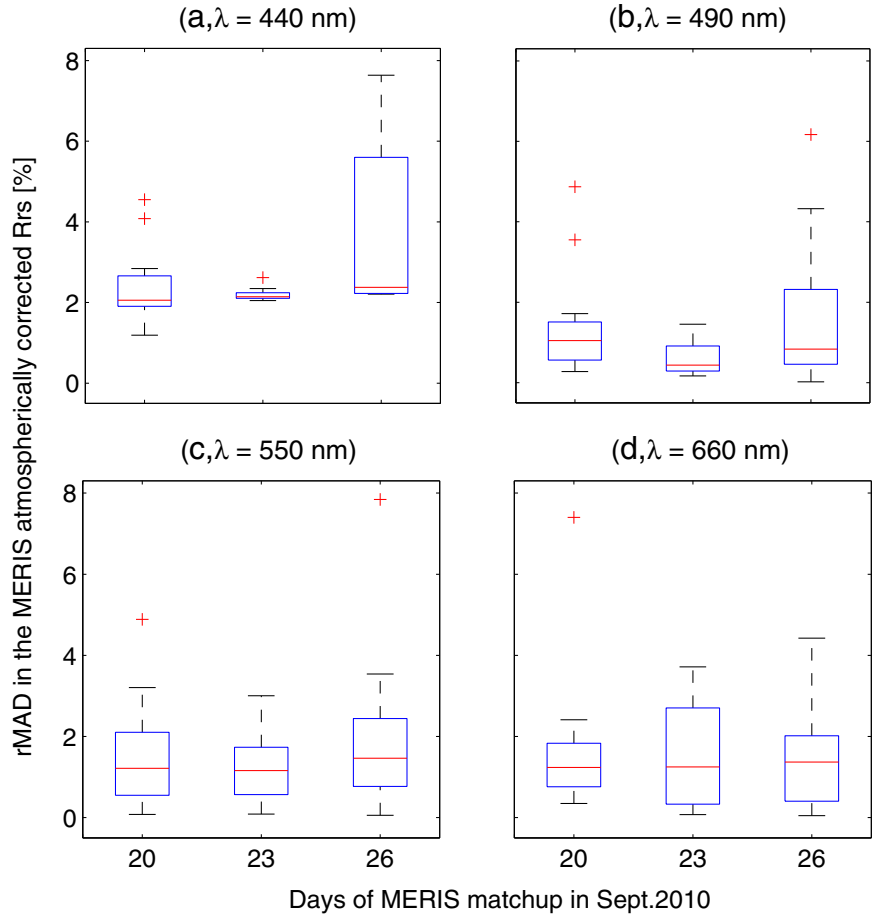

Fig. 5. The mean absolute relative error of remote sensing reflectance computed between field-measured and MERIS atmospherically corrected values. Four wavelengths are shown: (a) 440 nm, (b) 490 nm, (c) 550 nm and (d) 660 nm.

sets are selected such that they have the same moments (mean and standard deviation). The derived values of Rrs_a and T from the calibration sets are assumed to be spatially homogeneous over the lake for the time of the MERIS overpass. An evaluation of this method is shown in Fig. 5 for the validation sets and 4 visible bands of MERIS.

The largest errors (rMAD ~ 8%) and error variation (±3%) are found for the hazy conditions of the MERIS acquisitions on the 20th and 26th of September 2010. In general the average accuracy of the suggested atmospheric correction approach is less than 5% of rMAD. The best accuracy (small error ~1% and small variation of error ±0.4) is obtained at band 490 nm and for the MERIS image acquired on 23-09-2010, when clear sky conditions prevailed.

The spectral shape of the atmospheric correction errors is independent of the remote sensing spectra (*Rrs*), which confirms the validity of the used approach. The validation results of the atmospheric correction method followed in this paper are superior to those presented in our earlier work. In Majozi et al. (2014) we applied different atmospheric correction methods on the same data set and showed that the minimum obtained error in the remote sensing reflectance exceeded 40%.

5.2.2.2. Inversion of field and MERIS matchups. The 2SeaColor model is then applied to the field data (of Fig. 2-a) and the atmospherically corrected MERIS-matchups (34 matchup points). The derived K_d values are then compared to the measured ones (of Fig. 2-b) and shown in Fig. 6. In general, the retrieved values have a high degree of accuracy with errors, rMAD, less than 10% for both field data and MERIS matchups. Fig. 6-a shows that the retrieved $K_d(490)$ values from field data are 4% off unity with 0.17 m^{-1} intercept, high R^2 value >0.93 and small errors, rMAD ~ 4%. The retrievals from MERIS-matchups (Fig. 6-b) have larger deviation from the measured values (rMAD ~ 8%), but still relatively accurate, with 11% off unity slope at 0.6 m^{-1} intercept and 0.72 R^2 value.

6. Discussion

In this paper we propose 2SeaColor, a forward model with an inversion scheme, to derive the attenuation coefficient of turbid waters from remote sensing data. The model is verified and validated with simulated IOCCG data, *in situ* measurements and matchups from the MERIS sensor.

6.1. The model

6.1.1. Forward

The forward formulation of 2SeaColor provides an analytical and stable solution of the radiative transfer equation using the two-stream approximation. We proposed a modernized mathematical treatment of two-stream radiative transfer. We elaborate in more detail on the problem of numerical singularities in the calculation of directional reflectance and transmittance quantities.

The forward calculations of 2SeaColor produce irradiance reflectance values in the blue spectral range (440 nm) that are threefold more accurate than results from other models. This is due to the fact that in turbid water the scattering coefficient becomes more peaked in the forward direction. The referenced models use the quasi single scattering approximation (Gordon et al., 1975; Hansen, 1971), in which the forward scattering is totally neglected. In our treatment, we quantify the fraction of the most peaked forward scattering, and then transform the optical properties based on this value. In other words, the high turbidity common in inland waters is accounted for in 2SeaColor by projecting its effect on the IOPs.

The proposed 2SeaColor analytically derives the direct and diffuse components of downwelling irradiance as a function of IOPs. The weight factors of Gege (2012) can, however, be implemented in our model in computing downwelling irradiance.

These results present, to our knowledge, the first fully analytical treatment of depth profiles of the downward and upward fluxes.

6.1.2. Parameterization

We propose a novel approach to parameterize the spectral dependency of IOPs. In this parameterization, 2SeaColor uses the curvature information of observed remote sensing spectra to deduce the spectral-shape of the total absorption coefficient. As such, the 2SeaColor inversion scheme produces the exact shape and magnitude of the observed remote sensing spectra. The proposed parameterization has several advantages: (i) it guarantees that in the NIR spectral region water molecules are the only absorbing constituents; (ii) the produced spectrum fits the observed one; (iii) the effect of a pre-set chlorophyll-a parameterization (as related to phytoplankton type) on the spectral shape of the remote sensing reflectance is avoided; and (iv) the number of iterations required to obtain the best fit is reduced to ~10. One limitation of this parameterization is that the absorption coefficient is treated as a dumping parameter to follow the shape of the spectrum, affecting its accuracy.

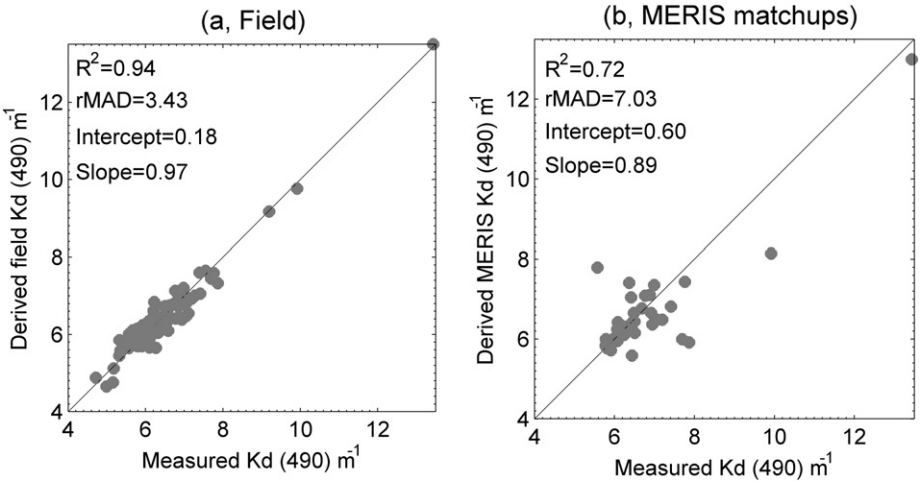

Fig. 6. $K_d(490)$ derived from 2SeaColor using measured field spectra (a) and observed MERIS remote sensing reflectances (b).

6.1.3. Inversion

The spectral optimization technique is used in the inversion scheme of 2SeaColor to derive the bulk absorption and backscattering coefficients and the depth profile of the downwelling attenuation coefficient in a homogenous water layer.

Since the produced radiometric quantity from 2SeaColor is the underwater irradiance reflectance and the observed quantity is the remote sensing reflectance (which can be transformed to under water) the Q ratio can also be computed. Although the capability to estimate the Q ratio has useful applications in turbid waters (Morel and Bélanger, 2006), it will increase the number of unknowns to five which might cause over fitting (Press et al., 2002).

The stability of the proposed inversion to sensor noise was analyzed by adding white noise to simulated spectra of the IOCCG data set. The noise is generated using the standard normal distribution with zero mean and standard deviation values equal to 5, 10, 15, 20 and 25% of reflectances in the IOCCG spectra. The imposed noise level is independent of wavelength. Table 3 shows the results of imposing different noise levels on the retrieved values of $K_d(490)$, $a(490)$ and $b_b(490)$. Derived values of $K_d(490)$ are stable up to a 15% noise level, where the error (rMAD) increases by a mere 5%, i.e. the effect of noise is dampened by a factor of three. This damping effect is less pronounced for $a(490)$, as the error increases by twofold for this noise level (15%).

This noise-filtering mechanism can be explained by three reasons. The first is due to computing K_d from the ratio of the downwelling irradiances at two depths, filtering out the noise. The second is due to the use of the similarity transform, whereby the peaked fraction is neglected. This fraction of the peaked forward scattering contains a large percentage of this noise. The third is due to the parameterization used, in which any change in the shape of the remote sensing reflectance is assigned to the absorption coefficient, which also explains why the absorption coefficient is the most affected by noise among others.

6.2. The validation

The attenuation coefficient (K_d) is calculated from the underwater downwelling planar irradiances measured at two depths, 0.2 and 0.7 m. We recognize, however, that accurate measurements at the upper point (0.2 m) are particularly difficult to make and the measurement of downwelling irradiance at two depths may not be sufficient to constrain the calculation of K_d. These factors could add more uncertainty to the validation exercise.

The remote sensing reflectance is computed from the ratio of measured water leaving radiance to the downwelling irradiance. The recorded radiance from the sea has to be corrected for the surface-reflected radiance from sun and sky in order to obtain the water-leaving radiance (Aas, 2010). In this study we did not correct *in situ* data for the reflected radiance at the water surface, which may have contributed to the total errors in the derived quantities. However, the presented sensitivity study of 2SeaColor inversion showed that the model is insensitive to noise up to a 15% noise level. The component of the radiance reflected at the water surface is, in general, less than 5%, which can be ignored in the computation of K_d due to the capability of 2SeaColor in filtering the noise out.

The $K_d(490)$ values in the simulated of IOCCG data range from 0 to 3.4 m^{-1}, whereas the range of the measured field values is between 3 m^{-1} and 12.5 m^{-1}. In terms of goodness of fit, the retrieved $K_d(490)$ values from the IOCCG data have larger errors (rMAD ~ 15%) than those derived from field measurements and MERIS matchups. Taking the ranges of these data sets into account, it can be stated that 2SeaColor is more appropriate for very turbid waters with $K_d(490) > 3$ m^{-1} and for clear waters with $K_d(490) < 1$ m^{-1}.

The good retrieval from MERIS matchups is attributed to the used method for atmospheric correction. This method is empirical in nature and based on field measurement of the water leaving remote sensing reflectance. In this sense, the regression between measured field values and top of atmosphere MERIS observations will reduce the influence of atmospheric correction errors on the retrievals. The remaining errors in MERIS matchup retrievals could be attributed to the local haze variation, the intrinsic model errors and spatial mismatch between point measurement and a pixel observation (Salama et al., 2011; Salama and Su, 2010, 2011).

On the other hand, derived IOPs of bulk absorption and backscattering coefficients have comparable accuracy (error < 15%) to other models when applied to the IOCCG data set (e.g. Salama and Shen, 2010a,b; Salama et al., 2009). It should be noted, however, that the current parameterization does not separate the absorption of the different water constituents. In this regard, 2SeaColor could benefit from further improvement in the parameterization and the inversion technique (e.g. Salama and Shen, 2010a).

7. Conclusions

We developed 2SeaColor, verified and validated it with simulated, field and satellite observed data sets. From the results of the analysis presented in this paper, we draw the following conclusions:

1. 2SeaColor applies an analytical solution of the radiative transfer using the two-stream approximation.
2. 2SeaColor projects the effect of turbidity on the IOPs and is therefore more suitable for deriving K_d in turbid waters than (quasi) single scattering models.
3. 2SeaColor is self-contained, stable to random noise and able to derive the depth profile of the downwelling attenuation coefficient in a homogenous water layer.
4. 2SeaColor gives consistently more accurate results in turbid waters and is therefore suitable for water quality retrievals in lakes from the future Ocean and Land Colour Instrument (OLCI) onboard of the Sentinel-3 mission.

Acknowledgement

This research was supported by the European Space Agency (ESA) under the Alcantara project "Ecological Modelling in the Nile Delta", Ref: 12-A14, Contract: AO/1-7102/12/F/MOS. The authors are indebted to the three anonymous reviewers for their comments.

Table 3
Sensitivity of 2SeaColor retrievals to random noise in the remote sensing reflectance of IOCCG data set.

Parameter	$K_d(490)$ at depth 0						$a(490)$						$b_b(490)$					
Noise %	0	5	10	15	20	25	0	5	10	15	20	25	0	5	10	15	20	25
Slope	1.14	1.15	1.18	1.26	1.38	1.56	1.12	1.15	1.32	1.61	1.69	2.14	1.10	1.12	1.24	1.43	1.40	1.50
Intercept	−0.04	−0.04	−0.05	−0.05	−0.07	−0.11	0.03	−0.03	−0.08	−0.15	−0.18	−0.33	0.00	0.00	0.00	−0.01	−0.01	−0.01
R^2	0.98	0.98	0.98	0.96	0.92	0.80	0.99	0.98	0.94	0.83	0.77	0.69	0.98	0.98	0.96	0.91	0.92	0.89
rMAD	11.84	12.62	14.50	18.88	24.67	29.48	10.76	11.71	15.97	22.05	28.29	36.80	10.70	10.93	12.98	15.84	17.14	19.67

Appendix A

We will assume here that of the total scattering coefficient b, a fraction is scattered backward (b_b) and a fraction is scattered forward (b_f)

$$b_b = \eta b \text{ and } b_f = (1-\eta)b, \tag{A.1}$$

where η is the backscattering fraction. The forward scattering coefficient is assumed to be composed of two components:

$$b_f = b_{fd} + b_{fp}. \tag{A.2}$$

The first component (b_{fp}) is concentrated in the forward peak with a fraction γ of the forward scattering:

$$b_{fp} = \gamma b_f. \tag{A.3}$$

The second component, b_{fd}, is still more diffuse and semi-isotropic (isotropic per hemisphere):

$$b_{fd} = (1-\gamma)b_f. \tag{A.4}$$

The equations needed for the similarity transformation are given by

$$\begin{aligned} c' &= c - b_{fp} = c - \gamma b_f = c - \gamma(1-\eta)b = c - \gamma(1-\eta)\omega c = [1-\gamma(1-\eta)\omega]c \\ \omega' &= \left(b - b_{fp}\right)/c' = \frac{\omega c[1-\gamma(1-\eta)]}{[1-\gamma(1-\eta)\omega]c} = \omega\frac{1-\gamma(1-\eta)}{1-\gamma(1-\eta)\omega} \\ \eta' &= b_b/\left(b - b_{fp}\right) = \omega\eta c/[\omega c - \gamma(1-\eta)\omega c] = \frac{\eta}{1-\gamma(1-\eta)} \end{aligned} \tag{A.5}$$

where c is the beam extinction coefficient and ω is the single scattering albedo. It can be verified that application of the above transformed optical properties gives back the correct scattering and absorption coefficients:

$$\begin{aligned} b_b &= \eta'\omega' c' = \eta\omega c \\ b_f &= (1-\eta')\omega' c' = (1-\gamma)(1-\eta)\omega c \\ a &= (1-\omega')c' = (1-\omega)c \end{aligned} \tag{A.6}$$

The extinction coefficient for sunlight is now given by

$$k = \frac{c'}{\cos\theta_s'}. \tag{A.7}$$

Appendix B

Table B.1 summarizes the coefficients of Eq. (1) which is solved as follows.

Table B.1
Summary of the coefficients used in Eq. (1).

Coefficients	Description	Relation
c	The extinction coefficient [m^{-1}]	$c = a + b$
k	The extinction coefficient for direct sunlight [m^{-1}]	$k = c/\mu_s$
s	backscattering scattering for direct sunlight [m^{-1}]	$s = b_b/\mu_s$
σ	diffuse backward scattering sunlight [m^{-1}]	$\sigma = 2b_b$
s'	forward scattering for direct sunlight [m^{-1}]	$s' = b_f/\mu_s$
σ'	diffuse forward scattering sunlight [m^{-1}]	$\sigma' = 2b_f$
α	The diffuse attenuation coefficient [m^{-1}]	$\alpha = 2a + 2b_b$

First, the direct solar flux is solved immediately as the exponential function $E_s(z) = E_s(0)e^{kz}$. For the solution of the diffuse fluxes we differentiate the diffuse downward flux of system (1) once more, giving

$$\begin{aligned} \frac{d^2E^-}{dz^2} &= -s'kE_s + \alpha\frac{dE^-}{dz} - \sigma\frac{dE^+}{dz} \\ &= -s'kE_s + \alpha\left[-s'E_s + \alpha E^- - \sigma E^+\right] - \sigma\left[sE_s + \sigma E^- - \alpha E^+\right] \\ &= -\left[s'(k+\alpha) + s\sigma\right]E_s + \left(\alpha^2 - \sigma^2\right)E^- \end{aligned} \tag{B.1}$$

As a general solution one can try

$$E^-(z) = p_1 e^{mz} + p_2 e^{-mz} + DE_s, \tag{B.2}$$

where p_1 and p_2 are constants which should follow from the boundary conditions, and the constant D and the coefficient m are found by differentiating the assumed general solution twice, which gives

$$\begin{aligned} \frac{d^2E^-(z)}{dz^2} &= m^2\left(p_1 e^{mz} + p_2 e^{-mz}\right) + k^2 DE_s = m^2[E^-(z) - DE_s] + k^2 DE_s \\ &= \left(k^2 - m^2\right)DE_s + m^2E^-(z) \end{aligned} \tag{B.3}$$

By equating this result to Eq. (B.1), one finds that $m^2 = \alpha^2 - \sigma^2$, so that m, the so-called eigenvalue of the system of differential equations, is given by

$$\begin{aligned} m &= \sqrt{\alpha^2 - \sigma^2} = \sqrt{(\alpha-\sigma)(\alpha+\sigma)} = \sqrt{2a(2a+4b_b)} \\ &= 2\sqrt{a(a+2b_b)}. \end{aligned} \tag{B.4}$$

It also follows that D must be given by

$$D = \frac{-\left[s'(k+\alpha) + s\sigma\right]}{k^2 - m^2}. \tag{B.5}$$

In the special case of a semi-infinite medium, which has no boundary at the bottom, the downward flux at a depth $z = -\infty$ must be assumed equal to zero, and the boundary constant p_2 then must be zero as well, so the solution becomes

$$E^-(z) = p_1 e^{mz} - \frac{\left[s'(k+\alpha) + s\sigma\right]}{k^2 - m^2}E_s(0)e^{kz}. \tag{B.6}$$

A well-known singularity occurs when $k = m$, in which case the constant D goes to infinity. This singularity case is also discussed in Verhoef and Bach (2007) for the vegetation reflectance model SLC (Soil–Leaf–Canopy), and the solution proposed there is applied in the present water model as well. In order to intercept the possible case of singularity, we write

$$\begin{aligned} E^-(z) &= p_1 e^{mz} - \frac{\left[s'(k+\alpha) + s\sigma\right]}{k^2 - m^2}E_s(0)\left[e^{kz} - e^{mz} + e^{mz}\right] \\ &= \left[p_1 - \frac{\left[s'(k+\alpha) + s\sigma\right]}{k^2 - m^2}E_s(0)\right]e^{mz} + \frac{\left[s'(k+\alpha) + s\sigma\right]}{k+m}E_s(0)\frac{e^{mz} - e^{kz}}{k-m} \\ &= \delta_1 e^{mz} + \frac{\left[s'(k+\alpha) + s\sigma\right]}{k+m}E_s(0)J_1(k,z) \end{aligned} \tag{B.7}$$

where δ_1 is a new boundary constant and J_1 is a function that is defined by

$$J_1(k,z) = \begin{cases} \dfrac{e^{mz} - e^{kz}}{k-m} & (k \neq m) \\ -ze^{kz} & (k = m) \end{cases} \tag{B.8}$$

Since $J_1(k,0) = 0$, the boundary constant δ_1 simply equals the diffuse incident downward flux at the top of the medium, $E^-(0)$, so that we can write

$$E^-(z) = E^-(0)e^{mz} + \frac{[s'(k+\alpha)+s\sigma]}{k+m}E_s(0)J_1(k,z). \quad (B.9)$$

In order to derive the upward diffuse flux, we return to system (1) and use again the differential equation for the diffuse downward flux, yielding

$$\sigma E^+ = -\frac{dE^-}{dz} - s'E_s + \alpha E^- \quad (B.10)$$

Since one can verify that $\frac{dJ_1}{dz} = mJ_1 - e^{kz}$, substitution gives

$$\frac{dE^-}{dz} = mE^- - \frac{[s'(k+\alpha)+s\sigma]}{k+m}E_s(0)e^{kz}, \quad (B.11)$$

so that

$$\begin{aligned}\sigma E^+ &= (\alpha - m)E^- + \left[\frac{[s'(k+\alpha)+s\sigma]}{k+m} - s'\right]E_s \\ &= (\alpha - m)E^- + \frac{s'(\alpha-m)+s\sigma}{k+m}E_s \end{aligned} \quad (B.12)$$

In particular, for the top of the medium we obtain

$$E^+(0) = \frac{\alpha-m}{\sigma}E^-(0) + \frac{s'\frac{\alpha-m}{\sigma}+s}{k+m}E_s(0) \quad (B.13)$$

One can also write this as

$$E^+(0) = r_\infty E^-(0) + \frac{s'r_\infty + s}{k+m}E_s(0), \quad (B.14)$$

where r_∞ is the so-called infinite reflectance, which is the bi-hemispherical reflectance for the semi-infinite medium. One can identify the expression $(s'r_\infty + s)/(k+m)$ as the directional-hemispherical reflectance of the semi-infinite medium, symbolized as r_{sd}^∞, so that one can finally write

$$E^+(0) = r_\infty E^-(0) + r_{sd}^\infty E_s(0). \quad (B.15)$$

Eq. (B.14) for the downward diffuse flux can now be further simplified to

$$\begin{aligned} E^-(z) &= E^-(0)e^{mz} + \frac{s'(k+\alpha)+s\sigma}{k+m}E_s(0)J_1(k,z) \\ &= E^-(0)e^{mz} + \frac{s'(k+m)+s'(\alpha-m)+s\sigma}{k+m}E_s(0)J_1(k,z) \\ &= E^-(0)e^{mz} + (s' + \sigma\ r_{sd}^\infty)E_s(0)J_1(k,z) \end{aligned} \quad (B.16)$$

The total downward flux of diffuse and direct light is:

$$E_d(z) = E^-(z) + E_s(0)e^{kz} \quad (B.17)$$

References

Aas, E. (2010). Estimates of radiance reflected towards the zenith at the surface of the sea. *Ocean Science*, *6*, 861–876.

Albert, A., & Mobley, C. (2003). An analytical model for subsurface irradiance and remote sensing reflectance in deep and shallow case-2 waters. *Optics Express*, *11*(22), 2873–2890.

Antoine, D., & Morel, A. (1999). A multiple scattering algorithm for atmospheric correction of remotely sensed ocean color (MERIS instrument): Principle and implementation for atmospheres carrying various aerosols including absorbing ones. *International Journal of Remote Sensing*, *20*, 1875–1916.

Austin, R. W., & Petzold, T. (1981). The determination of the diffuse attenuation coefficient of sea water using the Coastal Zone Color Scanner. In J. F. R. Gower (Ed.), *Oceanography from Space* (pp. 239–256). Plenum Press.

Ayenew, T., & Becht, R. (2008). Comparative assessment of the water balance and hydrology of selected Ethiopian and Kenyan rift lakes. *Lakes & Reservoirs: Research & Management*, *13*(3), 181–196.

Bilotta, G. S., & Brazier, R. E. (2008). Understanding the influence of suspended solids on water quality and aquatic biota. *Water Research*, *42*(12), 2849–2861.

Chomko, R. M., Gordon, H. R., Maritorena, S., & Siegel, D. A. (2003). Simultaneous retrieval of oceanic and atmospheric parameters for ocean color imagery by spectral optimization: A validation. *Remote Sensing of Environment*, *84*, 208–220.

Cox, C., & Munk, W. (1954a). Measurements of the roughness of the sea surface from photographs of the sun glitter. *Journal of Optical Society America*, *44*, 838–850.

Cox, C., & Munk, W. (1954b). Statistics of the sea surface derived from sun glitter. *Journal of Marin Research*, *13*, 198–227.

Devred, E., Sathyendranath, S., & Plat, T. (2007). Relationship between the Q factor and inherent optical properties: Relevance to ocean-colour inversion algorithms. *Geophysical Research Letters*, *34*, L18601.

Duntley, S. (1942). The optical properties of diffusing materials. *Journal of the Optical Society of America*, *32*(2), 61–70.

Duntley, S. (1963). Light in the sea. *Journal of the Optical Society of America*, *53*, 214–233.

Frouin, R., & Pelletier, B. (2007). Fields of non-linear regression models for atmospheric correction of satellite ocean-color imagery. *Remote Sensing of Environment*, *11*, 450–465.

Gege, P. (2012). Analytic model for the direct and diffuse components of downwelling spectral irradiance in water. *Applied Optics*, *51*(9), 1407–14019.

Giardino, C., Pepe, M., Brivio, P. A., Ghezzi, P., & Zilioli, E. (2001). Detecting chlorophyll, Secchi disk depth and surface temperature in a sub-alpine lake using Landsat imagery. *The Science of the Total Environment*, *268*(1–3), 19–29.

Gordon, H. (1997). Atmospheric correction of ocean color imagery in the Earth Observing System era. *Journal of Geophysical Research*, *102*, 17081–17106.

Gordon, H., Brown, O., Evans, R., Brown, J., Smith, R., Baker, K., et al. (1988). A semi-analytical radiance model of ocean color. *Journal of Geophysical Research*, *93*, 10,909–10,924.

Gordon, H. R., Brown, O. B., & Jacobs, M. M. (1975). Computed relationships between the inherent and apparent optical properties of a flat homogeneous ocean. *Applied Optics*, *14*(2), 417–427.

Gregg, W., & Carder, K. (1990). A simple spectral solar irradiance model for cloudless maritime atmospheres. *Limnology and Oceanography*, *35*, 1657–1675.

Hansen, J. E. (1971). Multiple scattering of polarized light in planetary atmospheres. *Part II. Sunlight reflected by terrestrial water clouds. Journal of Atmospheric Science*, *28*, 1400–1426.

Harper, D., Virani, M., Smart, A., Childress, R., Adatia, R., Henderson, I., et al. (2002). Population fluctuations and their causes in the African Fish Eagle, (Haliaeetus vocifer, Daudin) at Lake Naivasha, Kenya. *Hydrobiologia*, *488*(168), 171–180.

Kettle, H., & Merchant, C. (2008). Modeling ocean primary production: Sensitivity to spectral resolution of attenuation and absorption of light. *Progress in Oceanography*, *78*(2), 135–146.

Kirk, J. T. O. (1994). *Light and photosynthesis in aquatic ecosystems* (2nd ed.). Cambridge: Cambridge University Press.

Kopelevich, O. (1983). Small-parameter model of optical properties of sea waters. In A. Monin (Ed.), *Ocean Optics. Physical Ocean Optics, vol. 1.* (pp. 208–234). Nauka.

Kratzer, S., Brockmann, C., & Moore, G. (2008). Using MERIS full resolution data to monitor coastal waters — A case study from Himmerfjärden, a Fjord-like bay in the Northwestern Baltic Sea. *Remote Sensing of Environment*, *112*(5), 2284–2300.

Laws, E. (1997). *Mathematical methods for oceanographers: An introduction.* New York: John Wiley and Sons.

Lee, Z. (2006). *Remote sensing of inherent optical properties: Fundamentals, tests of algorithms, and applications.* Technical report 5. International Ocean-Colour Coordinating Group.

Lee, Z., Arnone, R., Hu, C., Werdell, J., & Lubac, B. (2010). Uncertainties of optical parameters and their propagations in an analytical ocean color inversion algorithm. *Applied Optic*, *49*(3), 369–381.

Lee, Z., Carder, K., & Arnone, R. (2002). Deriving inherent optical properties from water color: A multiband quasi-analytical algorithm for optically deep waters. *Applied Optics*, *41*, 5755–5772.

Lee, Z., Darecki, M., Carder, K. L., Davis, C. O., Stramski, D., & Rhea, W. J. (2005a). Diffuse attenuation coefficient of downwelling irradiance: An evaluation of remote sensing methods. *Journal of Geophysical Research*, *110*, C02017.

Lee, Z., Du, K., & Arnone, R. (2005b). A model for the diffuse attenuation coefficient of downwelling irradiance. *Journal of Geophysical Research*, C02016, http://dx.doi.org/10.1029/2004JC002275.

Lee, Z., Weidemann, A., Kindle, J., Arnone, R., Carder, K., & Davis, C. (2007). Euphotic zone depth: Its derivation and implication to ocean-color remote sensing. *Journal of Geophysical Research*, *112*, C03009.

Lewis, M. R., Carr, M. -E., Feldman, G. C., Esaias, W., & McClain, C. (1990). Influence of penetrating solar radiation on the heat budget of the equatorial Pacific Ocean. *Nature*, *347*(6293), 543–545.

Majozi, N., Salama, M. S., Bernard, S., Harper, D., & Ghirmai Habte, M. (2014). Remote sensing of euphotic depth in shallow tropical inland waters of Lake Naivasha using MERIS data. *Remote Sensing of Environment*, *148*, 178–189.

Manizza, M., Le Quere, C., Watson, A. J., & Buitenhuis, E. T. (2004). Bio-optical feedbacks among phytoplankton, upper ocean physics and sea-ice in a global model. *Geophysical Research Letters*, *32*, L05603.

Maritorena, S., Siegel, D., & Peterson, A. (2002). Optimization of a semi-analytical ocean color model for global-scale applications. *Applied Optics*, *41*, 2705–2714.

Mobley, C. D. (2004). *Light and water: Radiative transfer in natural waters.* Elsevier Science & Technology Books.
Morel, A., & Antoine, D. (1994). Heating rate within the upper ocean in relation to its bio-optical state. *Journal of Physical Oceanography*, *24*, 1652–1665.
Morel, A., & Bélanger, S. (2006). Improved Detection of turbid waters from Ocean Color information. *Remote Sensing of Environment*, *102*, 237–249.
Morel, A., & Gentili, B. (1991). Diffuse reflectance of oceanic waters: Its dependence on sun angle as influenced by the molecular scattering contribution. *Applied Optics*, *30*, 4427–4438.
Morel, A., & Gentili, B. (1996). Diffuse reflectance of oceanic waters. III. Implication of bidirectionality for the remote-sensing problem. *Applied Optics*, *35*, 4850–4862.
Mueller, J. (2000). *SeaWiFS algorithm for the diffuse attenuation coefficient, K (490), using water-leaving radiances at 490 and 555 nm.* SeaWiKS post-launch calibration and validation analyses*NASA technical memo*, *206892.* (pp. 11–24), 11–24.
Mueller, J. L., Morel, A., Frouin, R., Davis, C., Arnone, R., Carder, K., et al. (2003). *Ocean optics protocols for satellite ocean color sensor validation, revision 4.* Volume III: Radiometric measurements and data analysis protocols.
O'Reilly, J., Maritorena, S., Mitchell, B., Siegel, D., Carder, K., Kahru, L., et al. (1998). Ocean color algorithms for SeaWiFS. *Journal of Geophysical Research*, *103*, 24,937–24,953.
Pope, R., & Fry, E. (1997). Absorption spectrum (380-700 nm) of pure water: II, Integrating cavity measurements. *Applied Optics*, *36*, 8710–8723.
Preisendorfer, R. W. (1986). Secchi disk science: Visual optics of natural waters. *Limnology and Oceanography*, *31*, 909–926.
Press, W., Teukolsky, W., Vetterling, W., & Flannery, B. (2002). *Numerical recipes in C++, the art of scientific computing.* Cambridge U. Press.
Salama, M. S., Dekker, A. G., Su, Z., Mannaerts, C. M., & Verhoef, W. (2009). Deriving inherent optical properties and associated inversion-uncertainties in the Dutch lakes. *Hydrology and Earth System Sciences*, *13*(7), 1113–1121.
Salama, M. S., Melin, F., & Van der Velde, R. (2011). Ensemble uncertainty of inherent optical properties. *Optics Express*, *19*(18), 16772–16783.
Salama, M. S., Monbaliu, J., & Coppin, P. (2004). Atmospheric correction of advanced very high resolution radiometer imagery. *International Journal of Remote Sensing*, *25*(7–8), 1349–1355.
Salama, M. S., & Shen, F. (2010a). Simultaneous atmospheric correction and quantification of suspended particulate matters from orbital and geostationary earth observation sensors. *Estuarine, Coastal and Shelf Science*, *86*(3), 499–511.
Salama, M. S., & Shen, F. (2010b). Stochastic inversion of ocean color data using the cross-entropy method. *Optics Express*, *18*(2), 479–499.
Salama, M. S., & Stein, A. (2009). Error decomposition and estimation of inherent optical properties. *Applied Optics*, *48*(26), 4947–4962.
Salama, M. S., & Su, Z. (2010). Bayesian model for matching the radiometric measurements of aerospace and field ocean color sensors. *Sensors*, *10*(8), 7561–7575.
Salama, M. S., & Su, Z. (2011). Resolving the subscale spatial variability of apparent and inherent optical properties in ocean color match - up sites. *IEEE Transactions on Geoscience and Remote Sensing*, *49*(7), 2612–2622.
Salama, M. S., van der Velde, R., van der Woerd, H. J., Kromkamp, J. C., Philippart, C. J. M., Joseph, A. T., et al. (2012). Technical notes: Calibration and validation of geophysical observation models. *Biogeosciences*, *9*(6), 2195–2201.
Saulquin, B., Hamdi, A., Gohin, F., Populus, J., Mangin, A., & Fanton d'Andon, O. (2013). Estimation of the diffuse attenuation coefficient KdPAR using MERIS and application to seabed habitat mapping. *Remote Sensing of Environment*, *128*(21), 224–233.
Scheffer, M., Bascompte, J., Brock, W. A., Brovkin, V., Carpenter, S. R., Dakos, V., et al. (2009). Early-warning signals for critical transitions. *Nature*, *53*, 53–59.
Shen, F., Verhoef, W., Zhou, Yunxuan, Salama, M. S., & Xiaoli, L. (2010). Satellite estimates of wide - range suspended sediment concentrations in Changjiang, Yangtze estuary using MERIS data. *Estuaries and Coasts*, *33*(6), 1420–1429.
Tarras-Wahlberg, H., Everard, M., & Harper, D.M. (2002). Geochemical and physical characteristics of river and lake sediments at Naivasha, Kenya. *Hydrobiologia*, *488*(1–3), 27–41.
Uiboupin, R., & Sipelgas, L. (2007). Comparison of satellite sea surface temperature with *in situ* surface layer temperature. *Proceedings of the Estonian Academy of Sciences: Biology, Ecology*, *56*(1), 47–56.
Van de Hulst, H.C. (1981). Light Scattering by Small Particles. Wiley, NY, 1957; Dover, NY, 1981.
Van der Woerd, H., & Pasterkamp, R. (2008). Hydropt: A fast and flexible method to retrieve chlorophyll-a from multispectral satellite observations of optically complex coastal waters. *Remote Sensing of Environment*, *112*, 1795–1807.
Verhoef, W., & Bach, H. (2007). Coupled soil - leaf - canopy and atmosphere radiative transfer modeling to simulate hyperspectral multi - angular surface reflectance and TOA radiance data. *Remote Sensing of Environment*, *109*(2), 166–182.
Wang, P., Boss, E., & Roesler, C. (2005a). Uncertainties of inherent optical properties obtained from semianalytical inversions of ocean color. *Applied Optics*, *44*, 4074–4084.
Wang, M., & Gordon, H. R. (1994). A simple, moderately accurate, atmospheric correction algorithm for SeaWiFS. *Remote Sensing of Environment*, *50*, 231–239.
Wang, M., Knobelspiesse, K. D., & McClain, C. R. (2005b). Study of the Sea-Viewing Wide Field-of-View Sensor (SeaWiFS) aerosol optical property data over ocean in combination with the ocean color products. *Journal of Geophysical Research*, *110*, D10S06.
Wang, M., Son, S., & Shi, W. (2009). Evaluation of MODIS SWIR and NIR-SWIR atmospheric correction algorithm using SeaBASS data. *Remote Sensing of Environment*, *113*, 635–644.
Yang, W., Matsushita, B., Chen, Jin, Yoshimura, K., & Fukushima, T. (2013). Retrieval of inherent optical properties for turbid inland waters from remote-sensing reflectance. *IEEE Transactions on Geoscience and Remote Sensing*, *51*(6), 3761–3773.
Zibordi, Z., & Berthon, J. -F. (2001). Relationships between Q-factor and seawater optical properties in a coastal region. *Limnology and Oceanography*, *46*(5), 1130–1140.